
Article:
Dickson, L. T., Moulanier, I., Massimo, F. et al. (2025) Spectral phase control for optimized ionization injection in laser wakefield acceleration. Physical Review Accelerators and Beams. 121301. ISSN: 2469-9888

https://doi.org/10.1103/9gjq-htzn

Spectral phase control for optimized ionization injection in laser wakefield acceleration

M. P. Backhouse,[1,*] L. T. Dickson,[2,3] I. Moulanier,[2] F. Massimo,[2] C. C. Cobo,[1,4] F. Filippi,[5] C. Gustafsson,[6] E. Lofquist,[6] K. Svendsen,[6] M. J. V. Streeter,[1,7] R. J. Shalloo,[1,8] O. Vasilovici,[2] C. Ballage,[2] S. J. D. Dann,[9] C. D. Murphy,[4] Z. Najmudin,[1] S. Dobosz Dufrénoy,[10] O. Lundh,[6] and B. Cros[2]

[1]*The John Adams Institute for Accelerator Science, Imperial College, London, SW7 2BZ, United Kingdom*
[2]*LPGP, CNRS, 91405, Orsay, France*
[3]*Department of Electronic and Electrical Engineering, University of Strathclyde, Glasgow, G1 1RD, United Kingdom*
[4]*York Plasma Institute, School of Physics, Engineering and Technology, University of York, Heslington, York, YO10 5DD, United Kingdom*
[5]*ENEA, Nuclear Department—C. R. Frascati, Via Enrico Fermi 45, 00044, Frascati, Italy*
[6]*Department of Physics, Lund University, Lund SE-221 00, Sweden*
[7]*School of Mathematics and Physics, Queen's University Belfast, Belfast BT7 1NN, United Kingdom*
[8]*Deutsches Elektronen-Synchrotron DESY, D-22607 Hamburg, Germany*
[9]*Central Laser Facility, Rutherford Appleton Laboratory, Didcot, OX11 0QX, United Kingdom*
[10]*LIDYL, Université Paris Saclay, CEA, Saclay, France*

(Received 9 May 2025; accepted 31 October 2025; published 1 December 2025)

Generating narrow energy spread beams from laser wakefield accelerators with minimal dark current is important for many applications. We present an automated experiment using Bayesian optimization to control the laser spectral phase and focal position, achieving significant enhancement of the beam quality. Starting from a broadband spectrum, the optimized configuration achieved low-energy spread with negligible dark current above 20 MeV. Particle-in-cell simulations reveal that fine control over the laser spectral phase, particularly third-order dispersion, directly impacts the timing and localization of ionization injection due to its effect on the initial laser intensity envelope and its subsequent evolution. A positively skewed temporal profile enhances the plasma potential depth at the right location, enabling localized injection and reducing the energy spread and dark current. These findings highlight the impact of algorithmic optimization and the powerful, underutilized role of temporal shaping in beam quality control.

DOI: 10.1103/9gjq-htzn

Laser wakefield acceleration (LWFA) [1–3] has become a commonly used tool for compactly generating relativistic electron beams. A tightly focused high-intensity laser pulse propagating through an underdense plasma can excite large amplitude plasma waves in its wake that can trap and accelerate particles to GeV energies over mere centimeters [4]. The laser itself can be used to inject particles into the wake, either by exciting the plasma oscillation to the point of wave breaking [5–7] or by freeing tightly bound electrons within the trapping phase of the wake [8–14]. The microscopic length scales and large accelerating gradients permit low-emittance beams [15,16]. This makes laser wakefield accelerators attractive as injectors for multistage accelerators [17–20].

In uncontrolled injection regimes, electron beams produced by LWFA often have energy spreads approaching 100%. In contrast, beams with low-energy spread and minimal dark current are preferred for their ease of transport and suitability for applications [21,22]. Tailoring the plasma density profile longitudinally can reduce the energy spread by restricting the region where injection occurs, but maximizing performance typically requires fine-tuning of experimental input parameters. In many operating modes, the electron spectrum is highly sensitive to these variables, so achieving optimal performance represents a multidimensional optimization problem. Further, beam time limitations, low laser repetition rates, and shot-to-shot variability impose significant cost and noise on the measurements.

Bayesian optimization (BO) is well suited to this problem [23,24]. Previous work using BO to improve

*Contact author: michael.backhouse13@imperial.ac.uk

LWFA performance has focused on either optimizing for smoothly varying beam metrics, such as charge or x-ray flux from betatron radiation [23], or on improving the spectral density of a beam within the narrow energy range of an imaging spectrometer [24]. Simultaneous optimization of multiple objectives presents the problem of how much importance to give to the competing beam metrics. This may be dealt with by using multiobjective formulations [25,26], where a series of optimal tradeoffs are located. This approach has the benefit of flexibility but may be inappropriate when sample efficiency is paramount. What remains to be demonstrated is the implementation of BO in the standard LWFA setting to control energy spread, without assistance from advanced targetry or imaging spectrometers, which make the production and detection of low-energy spread beams much easier. Demonstrating the use of algorithms to condition beams for applications with a simple experimental setup and input parameters that are readily available on almost every laser system has the potential to catalyze the widespread adoption of LWFA for applications.

In this Letter, we show that BO can rapidly maximize electron beam spectral density, reduce energy spread, and eliminate dark current simultaneously by controlling the spectral phase of the laser pulse and its focal position. Critically, these results were achieved without the assistance of an imaging spectrometer, forcing the optimization to start from 100% energy spread. By incorporating multiple electron beam parameters into a single objective, optimal performance was achieved in a highly sample-efficient manner. The close matching between particle-in-cell (PIC) simulations and the experiment [27] allows us to show how the spectral phase terms of the laser were critical for maximizing the charge in the beam while eliminating dark current. These results demonstrate how to use BO to perform the vital task of generating low-energy spread, low dark current beams, and further show the key role the spectral phase terms play in maximizing performance.

The experiment used the Lund Laser Centre laser [28], which focused $\lambda_0 = 800$ nm, 0.8 J, 42 fs (FWHM) laser pulses to a $1/e^2$ spot size of 12 μm. A 32-actuator [NightN (opt) Ltd.] adaptive optic was used with a Phasics SID4 wave front sensor to reduce spatial phase variations and optimize the focal spot. Hydrogen gas doped with nitrogen at a concentration of 5% by mass was used as the acceleration medium. The ELISA gas cell [29,30] was used to contain the target gas mix and could be modified manually to alter the plateau, entrance, and exit plasma scale-lengths. Transverse optical probing of the cell was used to measure the peak plasma density in the plateau region through interferometry; the best electron beams were obtained using densities in the $(3.4\text{–}7.4) \times 10^{18}$ cm^{-3} range. The electron spectrometer was composed of a 20 cm, 0.8 T permanent dipole magnet and a LANEX scintillating screen, imaged onto a 16-bit CCD. The laser was linearly polarized in the magnet dispersion plane. Measurement of the imaging line optical efficiency using a continuous wave laser of known power allowed for an absolute charge calibration [31]. The error on the peak electron energy was determined by calculating the effects of pointing fluctuations into the magnet at different energies within the angular acceptance, amounting to a maximum of 1.2% at 150 MeV.

Automated Bayesian optimization [32] was performed using the longitudinal focal position of the laser and the second, third, and fourth-order spectral phase terms to define the search space. A standard BO setup was implemented, where a homoskedastic Gaussian process with a Matérn $\nu = 3/2$ kernel plus a white noise kernel was used to model the interaction [33], expected improvement was used as the acquisition function, and SCIKIT-LEARN and SCIKIT-OPTIMIZE were used for the kernel fitting and optimization, respectively [34]. The acquisition function was optimized by sampling it along random lines passing through previous sample points. The coordinates with the highest expected improvement were used for the next measurement location.

The spectral phase $\psi(\omega)$ represents the phase in the frequency domain. It is defined by its Taylor expansion [35]: $\psi(\omega) = \sum_{n=0}^{N} \beta^{(n)}/(n!)(\omega - \omega_0)^n$, where ω_0 is the laser carrier frequency and $\beta^{(n)} = \partial^n \psi/\partial\omega^n|_{\omega=\omega_0}$ is the spectral phase parameter of the nth order. Spectral phase was modified using a Fastlite Dazzler. The longitudinal focal position relative to the gas cell, f, was measured by imaging a 50-μm-thick needle. The position of the focal plane was determined by measuring the width of the focal spot as a function of position, from which a quadratic fit could determine the absolute position. This allowed f to be determined within ±200 μm.

The merit of a given electron beam was calculated using $\mathcal{S} = \sqrt{Q}\,E/\Delta E$ Ref. [24], where Q is the charge in the peak, ΔE is the full width at half maximum, and E is the energy at which dQ/dE is maximal. The metric was calculated only when $\max(dQ/dE) > 3\sigma_s$, with σ_s the standard deviation of the spectral background; otherwise, $\mathcal{S}$ was set to zero. If the spectrum did not fall by more than 50% between the $\max(dQ/dE)$ energy and the spectrometer lower limit, then a width of double the upper half-width value was used for ΔE. This provided a smooth transition from evaluating large energy spread beams to progressively narrower spectra.

Figure 1(a) shows $\mathcal{S}$ during the initial random shots (I), the optimization process (II), and the shots taken after optimization (III). During (I), a high charge, large energy spread beam was consistently produced while the inputs varied randomly, indicating that this regime was robust to substantial parameter variation. Examples of these beams are shown in Fig. 1(f). At the start of the optimization process, modest changes to the input parameters were made as a regime for improving the score was quickly identified

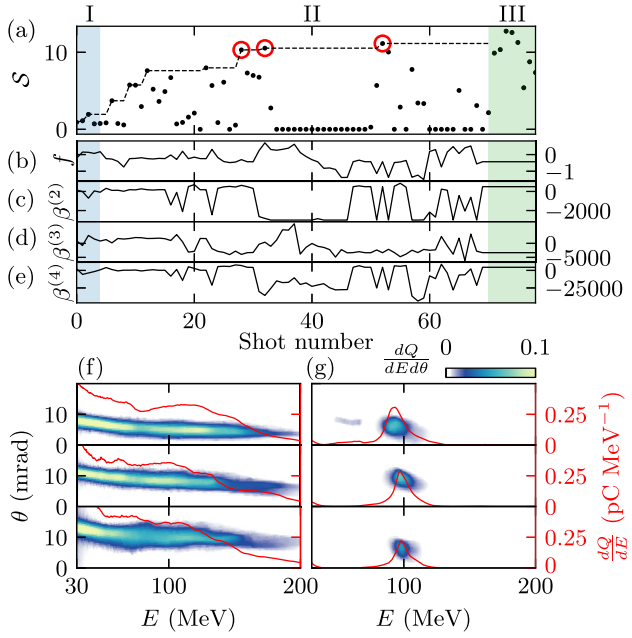

FIG. 1. (a) Spectral density metric $\mathcal{S}$ (units $\sqrt{\text{pC}}$) before (I), during (II), and after (III) Bayesian optimization. (b)–(e) change in input parameters during the optimization, where f is the focal position (units mm) and $\beta^{(n)}$ is the nth spectral phase term (units fs^n). (f) Processed electron spectrometer images taken from the initial random sample. (g) Highlighted low-energy spread beams recorded during optimization correspond to the red circles in (a). The color scale units are pC MeV^{-1} mrad^{-1}.

and exploited. From shot 16, the algorithm switched to a more explorative mode, after which a regime that allowed further improvements was located and exploited during shots 25–32. Two of these electron beam shots are shown in Fig. 1(g). From there, the algorithm conducted further explorations of the parameter space, resulting in shots that produced no measurable electron beams. After a period of exploration, the optimizer returned to the optimal location and generated the final beam in Fig. 1(g).

The optimizer outperformed manual sequential 1D scans performed by the experimenters, which makes the located configuration likely to be close to the global optimum within the variable ranges used. The best performance was found by focusing before the gas cell, $f = -0.5$ mm, and by using a slightly stretched pulse with positive skew, $(\beta^{(2)}, \beta^{(3)}, \beta^{(4)}) = (501\ \text{fs}^2, -3317\ \text{fs}^3, 4485\ \text{fs}^4)$. To investigate the stability of this optimum a series of 9 shots were taken, producing the beams seen in Fig. 2. The peak energy fluctuated by 5% rms, while Q varied by 40%. The value of the optimization metric varied by 20%; $\mathcal{S} = (11 \pm 2)\sqrt{\text{pC}}$, with $\Delta E_{\text{FWHM}} = (13 \pm 2)$ MeV. The relatively reduced variation of $\mathcal{S}$ results from a correlation between Q and ΔE_{FWHM}, which has a Pearson coefficient of 0.5.

Simulations were performed to investigate the injection and acceleration processes using the particle-in-cell

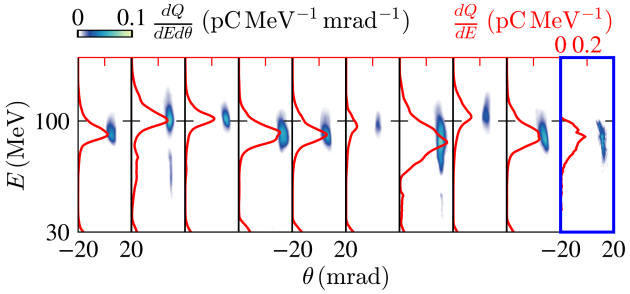

FIG. 2. Repeated shots at the optimal location [section III in Fig. 1(a)]. The rightmost spectrum, framed in blue, shows the simulation output with the experimentally optimal parameters.

code FBPIC [36]. A moving window with dimensions $(110, 140\ \mu\text{m})$ was used, with a resolution of $(32, 2)/\lambda_0$ in the (z, r) directions, retaining 5 azimuthal modes [37], defined in a Lorentz-boosted frame [38], $\gamma_b = 1.5$. The longitudinal density profile was determined using fluid simulation [29], and was simulated using $2 \times 2 \times 16$ macroparticles $(z \times r \times \theta)$. The laser was modeled with a transverse intensity and phase profile that matched the experiment. This was achieved by imaging the focal volume and applying the Gerchberg-Saxton algorithm with mode decomposition [39,40]. The laser spectral phase terms and the transverse electric field profile were then initialized using the experimentally determined optimal values. The rightmost frame of Fig. 2 shows the electron beam at the end of the simulation. The main features of the experimental measurement are reproduced well: an off-axis positive exit angle of 12 mrad, compared to 8 mrad in experiment, and a central energy of 88 MeV, compared to 90 MeV. The close agreement implies that the simulations model the physics of the interaction accurately, and may be used to investigate the mechanism by which the low-energy spread beams are produced.

Determining the effect of each parameter on the ultimate electron spectrum is challenging due to the couplings between them and the nonlinear nature of the interaction. To gain some insight, we performed simulations to scan the values of $\beta^{(2)}$ and $\beta^{(3)}$ around their respective optima, with the final electron spectra plotted in Figs. 3(a) and 3(b). Here the resolution was $(25, 2)/\lambda_0$ with $\gamma_b = 3$. The chirp parameter $\beta^{(2)}$, Fig. 3(a), has the strongest effect on the spectrum; a slight decrease from the optimum results in a large amount of charge being injected but with a broadband energy spectrum, while a slight increase results in no electron beam being produced. This is primarily due to the changes to peak initial laser intensity, which are plotted in red circles against the right axis. Changes to third-order dispersion, $\beta^{(3)}$, preserve the peaked spectrum but modify the width and the total charge injected. Both $\beta^{(2)}$ and $\beta^{(3)}$ alter the initial laser intensity significantly. Observe that the peak electron energy correlates strongly with a_0, as does the total amount of charge. These effects are unsurprising,

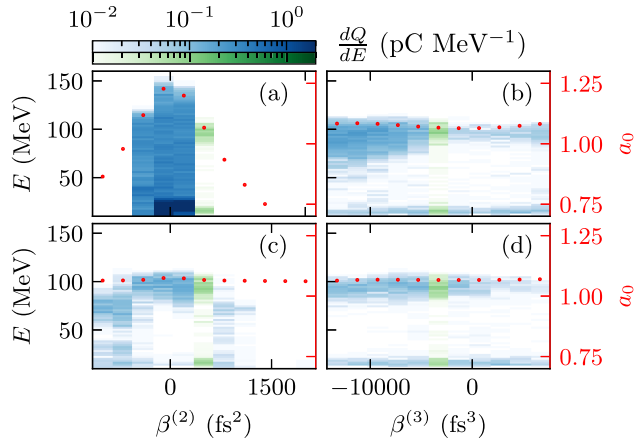

FIG. 3. Electron spectra from simulations performed with input parameters close to the experimentally found optimum. (a), (b) $\beta^{(2)}$ and $\beta^{(3)}$ parameter scans, (c),(d) $\beta^{(2)}$ and $\beta^{(3)}$ parameter scans with the initial a_0 matched to the start of simulations using the optimum parameters. The green color bar highlights the spectrum at the optimum coordinates. The red dots are the initial laser peak a_0.

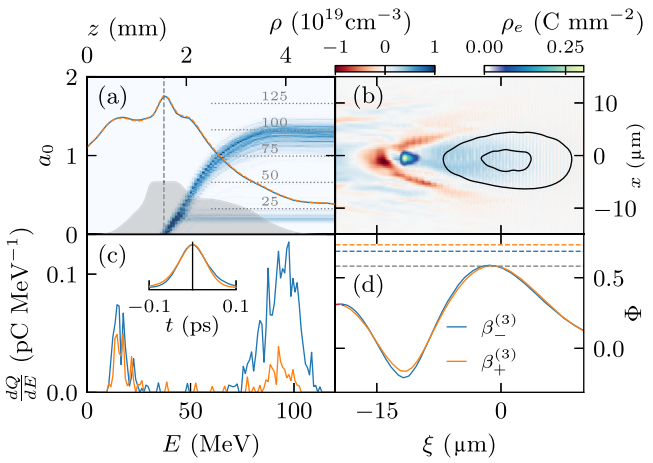

FIG. 4. Simulation comparison for $\beta_-^{(3)} = -7000$ fs^3 and $\beta_+^{(3)} = 7000$ fs^3. (a) The evolution of laser a_0 in each simulation (blue and orange lines), compared to the axial density profile in gray and the evolution of the electron spectrum in MeV (blue colormap with range [0–0.2] pC MeV^{-1}). (b) Snapshot at the peak a_0 value from the $\beta_-^{(3)}$ simulation, indicated by the dashed vertical line in (a). The field data is sliced at $y = -1$ μm to include the wake axis, which is slightly off-center due to the asymmetric laser intensity profile. The background shows a map of the plasma density, ρ, and the foreground shows a density map of the trapped electrons, ρ_e, integrated in y. The $a_0 = 1$ and 1.5 contours of the laser pulse are plotted in black. (c) The spectra at the final z position from each simulation. The inset shows the initial laser envelopes with the leading edge on the $t > 0$ side. (d) The electrostatic potentials from the two simulations at the peak a_0. The horizontal dashed lines show the trapping threshold, for each potential, while the gray dashed line shows the threshold as the wake velocity decreases during injection.

since increased a_0 strengthens the plasma wave and exponentially increases the ionization rate. Altering the intensity also modifies the dynamics of the laser-plasma interaction by changing the rate of self-focusing and the amplitude of the plasma wave.

To isolate the effect of modifying the pulse shape, further scans were run using the same parameters but with initial a_0 values matched to the optimum, shown in Figs. 3(c) and 3(d). This would be equivalent to making the spectral phase modifications with commensurate changes in laser energy. The spectral phase alterations strongly affect the electron spectrum independently of the laser intensity. The chirp values near zero produce the most energetic and highest spectral density beams, while negative values of third-order dispersion result in improved beam parameters. The effect of chirp is predictable due to the shorter pulse providing a larger ponderomotive force. The influence of third-order dispersion is more subtle and requires further investigation.

Figure 4 explains the effect of the changes in third-order dispersion. Figure 4(a) shows the evolution of the electron beam spectrum, the laser a_0, and the axial density profile of the target. The laser focuses before the plateau, moderating the intensity with which it enters the high-density region. Relativistic self-focusing and diffraction then cause the laser a_0 to increase and then decrease, producing the bump in intensity that can be seen in the region 1.5 mm $< z <$ 2 mm. The intensity then drops monotonically due to diffraction as the plasma density decreases, preventing further injection.

Electrons are injected via ionization injection during the intensification of the laser in the high-density region, and this localization of the injection process is responsible for the reduced energy spread. The correct vacuum focal position of the laser is vital: focusing closer to the plateau increases the laser intensity and leads to continuous electron injection into the wake, whereas focusing further away makes the wake too weak to trap electrons. The initial diffraction following the intensity peak at $z = 1.5$ mm is critical to reducing dark current since this causes the plasma wave to decrease in length slightly, resulting in electrons with an insufficiently advanced phase falling out of the accelerating region. Some of these electrons are observed at the low-energy end of the spectrum, in both the experimental measurements and the simulations. The laser a_0 evolution is almost identical for both the $\beta_-^{(3)}$ and $\beta_+^{(3)}$ cases and does not explain the difference between the final spectra seen in Fig. 4(c).

The simulations show that a positively skewed laser temporal profile is critical for maximizing performance. Figure 4(d) plots the axial normalized potential of the plasma wave, $\Phi = e\phi/(m_e c^2)$, where ϕ is the potential, calculated by integrating the longitudinal electric field along the wake axis. The trapping condition requires that an electron ionized at phase ξ_i must satisfy

$\Phi(\xi_i) \geq 1 - \sqrt{1+a_0^2}/\gamma_p + \Phi_{\min}$, where γ_p is the Lorentz factor of the wake and $\Phi_{\min}$ is the minimum of the potential [10,11]. The blue and orange horizontal dashed lines correspond to the trapping threshold for the $\beta_-^{(3)}$ and $\beta_+^{(3)}$ simulations, respectively, using $\gamma_p = (1-(v_g/c)^2)^{-1/2}$, where v_g is the group velocity of the laser. The gray dashed line is the $\beta_-^{(3)}$ simulation threshold calculated using $\gamma_p = \gamma_{p,\min} \simeq 10$, which occurs while a_0 increases rapidly at $z = 1.7$ mm. This was measured relative to v_g by tracking the position of the back of the first accelerating region of the plasma wave. For both the $\beta_-^{(3)}$ and $\beta_+^{(3)}$ simulations, injection only occurs during the suppression of the threshold. The $\beta_-^{(3)}$ pulse drives a slightly stronger plasma wave with a deeper potential that traps electrons earlier, resulting in a larger number of electrons with a more advanced phase. In this way, the small difference between the laser temporal envelopes results in a significant difference in the number of electrons injected early enough to remain in the accelerating phase of the wake.

In summary, we have shown that Bayesian optimization using only laser parameters as input variables can increase spectral density, reduce energy spread, and reduce dark current density over a large spectral range. The optimum regime produced beams with exceptionally low dark current and was robust to fluctuations in the input parameters when taking repeated shots. Accurate modeling of the laser spatial phase and intensity profile allowed PIC simulation results to reproduce the experimental measurements closely. The electron beam improvements were achieved by controlling the laser focus and pulse width such that the laser intensity briefly peaked in the high-density region of the density profile, and then by tuning the skew of the pulse to maximize the plasma wave amplitude during injection. These findings highlight the underutilized power of temporal shaping in tuning beam quality and support the use of Bayesian optimization for sample-efficient control of complex laser-plasma interactions in next-generation accelerator systems.

ACKNOWLEDGMENTS

This project has received funding from the European Union's Horizon 2020 Research and Innovation Programme under Grant Agreement No. 730871. We acknowledge funding from STFC (ST/J002062/1, ST/P002021/1, and ST/V001639/1), from DSTL/EPSRC (EP/S513635/1). We acknowledge support from the Knut and Alice Wallenberg Foundation (Grants No. KAW 2019.0318, No. 2020.0111), the Swedish Research Council (Grants No. 2019-04784, No. 2024-05698), and support from the Royal Society URF-R1221874. I. M. was supported by the CNRS in the framework of the project DIANA, Contract No. 1255841.

DATA AVAILABILITY

The data that support the findings of this article are not publicly available upon publication because it is not technically feasible and/or the cost of preparing, depositing, and hosting the data would be prohibitive within the terms of this research project. The data are available from the authors upon reasonable request.

[1] T. Tajima and J. M. Dawson, Phys. Rev. Lett. **43**, 267 (1979).
[2] F. Amiranoff, S. Baton, D. Bernard, B. Cros, D. Descamps, F. Dorchies, F. Jacquet, V. Malka, J. R. Marquès, G. Matthieussent, P. Miné, A. Modena, P. Mora, J. Morillo, and Z. Najmudin, Phys. Rev. Lett. **81**, 995 (1998).
[3] E. Esarey, C. B. Schroeder, and W. P. Leemans, Rev. Mod. Phys. **81**, 1229 (2009).
[4] A. Picksley, J. Stackhouse, C. Benedetti, K. Nakamura, H. E. Tsai, R. Li, B. Miao, J. E. Shrock, E. Rockafellow, H. M. Milchberg, C. B. Schroeder, J. van Tilborg, E. Esarey, C. G. R. Geddes, and A. J. Gonsalves, Phys. Rev. Lett. **133**, 255001 (2024).
[5] S. P. D. Mangles, C. D. Murphy, Z. Najmudin, A. G. R. Thomas, J. L. Collier, A. E. Dangor, E. J. Divall, P. S. Foster, J. G. Gallacher, C. J. Hooker, D. A. Jaroszynski, A. J. Langley, W. B. Mori, P. A. Norreys, F. S. Tsung, R. Viskup, B. R. Walton, and K. Krushelnick, Nature (London) **431**, 535 (2004).
[6] C. G. R. Geddes, C. Toth, J. van Tilborg, E. Esarey, C. B. Schroeder, D. Bruhwiler, C. Nieter, J. Cary, and W. P. Leemans, Nature (London) **431**, 538 (2004).
[7] J. Faure, Y. Glinec, A. Pukhov, S. Kiselev, S. Gordienko, E. Lefebvre, J. P. Rousseau, F. Burgy, and V. Malka, Nature (London) **431**, 541 (2004).
[8] T. P. Rowlands-Rees, C. Kamperidis, S. Kneip, A. J. Gonsalves, S. P. D. Mangles, J. G. Gallacher, E. Brunetti, T. Ibbotson, C. D. Murphy, P. S. Foster, M. J. V. Streeter, F. Budde, P. A. Norreys, D. A. Jaroszynski, K. Krushelnick, Z. Najmudin, and S. M. Hooker, Phys. Rev. Lett. **100**, 105005 (2008).
[9] C. McGuffey, A. G. R. Thomas, W. Schumaker, T. Matsuoka, V. Chvykov, F. J. Dollar, G. Kalintchenko, V. Yanovsky, A. Maksimchuk, K. Krushelnick, V. Y. Bychenkov, I. V. Glazyrin, and A. V. Karpeev, Phys. Rev. Lett. **104**, 025004 (2010).
[10] A. Pak, K. A. Marsh, S. F. Martins, W. Lu, W. B. Mori, and C. Joshi, Phys. Rev. Lett. **104**, 025003 (2010).
[11] M. Chen, E. Esarey, C. B. Schroeder, C. G. R. Geddes, and W. P. Leemans, Phys. Plasmas **19**, 033101 (2012).
[12] M. Mirzaie, S. Li, M. Zeng, N. A. M. Hafz, M. Chen, G. Y. Li, Q. J. Zhu, H. Liao, T. Sokollik, F. Liu, Y. Y. Ma, L. M. Chen, Z. M. Sheng, and J. Zhang, Sci. Rep. **5**, 14659 (2015).
[13] A. Irman, J. P. Couperus, A. Debus, A. Köhler, J. M. Krämer, R. Pausch, O. Zarini, and U. Schramm, Plasma Phys. Controlled Fusion **60**, 044015 (2018).

[14] M. Kirchen, S. Jalas, P. Messner, P. Winkler, T. Eichner, L. Hübner, T. Hülsenbusch, L. Jeppe, T. Parikh, M. Schnepp, and A. R. Maier, Phys. Rev. Lett. **126**, 174801 (2021).
[15] S. Kneip, C. McGuffey, J. L. Martins, M. S. Bloom, V. Chvykov, F. Dollar, R. Fonseca, S. Jolly, G. Kalintchenko, K. Krushelnick, A. Maksimchuk, S. P. D. Mangles, Z. Najmudin, C. A. J. Palmer, K. T. Phuoc, W. Schumaker, L. O. Silva, J. Vieira, V. Yanovsky, and A. G. R. Thomas, Phys. Rev. ST Accel. Beams **15**, 021302 (2012).
[16] R. Weingartner, S. Raith, A. Popp, S. Chou, J. Wenz, K. Khrennikov, M. Heigoldt, A. R. Maier, N. Kajumba, M. Fuchs, B. Zeitler, F. Krausz, S. Karsch, and F. Grüner, Phys. Rev. ST Accel. Beams **15**, 111302 (2012).
[17] B. B. Pollock, C. E. Clayton, J. E. Ralph, F. Albert, A. Davidson, L. Divol, C. Filip, S. H. Glenzer, K. Herpoldt, W. Lu, K. A. Marsh, J. Meinecke, W. B. Mori, A. Pak, T. C. Rensink, J. S. Ross, J. Shaw, G. R. Tynan, C. Joshi, and D. H. Froula, Phys. Rev. Lett. **107**, 045001 (2011).
[18] P. A. Walker *et al.*, J. Phys. Conf. Ser. **874**, 012029 (2017).
[19] S. Steinke, J. van Tilborg, C. Benedetti, C. G. R. Geddes, C. B. Schroeder, J. Daniels, K. K. Swanson, A. J. Gonsalves, K. Nakamura, N. H. Matlis, B. H. Shaw, E. Esarey, and W. P. Leemans, Nature (London) **530**, 190 (2016).
[20] T. Kurz *et al.*, Nat. Commun. **12**, 2895 (2021).
[21] F. Albert and A. G. R. Thomas, Plasma Phys. Controlled Fusion **58**, 103001 (2016).
[22] R. W. Assmann *et al.*, Eur. Phys. J. Special Topics **229**, 3675 (2020).
[23] R. J. Shalloo *et al.*, Nat. Commun. **11**, 6355 (2020).
[24] S. Jalas, M. Kirchen, P. Messner, P. Winkler, L. Hübner, J. Dirkwinkel, M. Schnepp, R. Lehe, and A. R. Maier, Phys. Rev. Lett. **126**, 104801 (2021).
[25] F. Irshad, S. Karsch, and A. Döpp, Phys. Rev. Res. **5**, 013063 (2023).
[26] F. Irshad, C. Eberle, F. M. Foerster, K. v. Grafenstein, F. Haberstroh, E. Travac, N. Weisse, S. Karsch, and A. Döpp, Phys. Rev. Lett. **133**, 085001 (2024).
[27] C. K. Birdsall and A. B. Langdon, *Plasma Physics via Computer Simulation* (Taylor and Francis Group, London, 2004).
[28] B. Aurand, M. Hansson, L. Senje, K. Svensson, A. Persson, D. Neely, O. Lundh, and C.-G. Wahlström, Laser Part. Beams **33**, 59 (2015).
[29] T. Audet, P. Lee, G. Maynard, S. D. Dufrénoy, A. Maitrallain, M. Bougeard, P. Monot, and B. Cros, Nucl. Instrum. Methods Phys. Res., Sect. A **909**, 383 (2018).
[30] L. Dickson, C. Underwood, F. Filippi, R. Shalloo, J. B. Svensson, D. Guénot, K. Svendsen, I. Moulanier, S. D. Dufrénoy, C. Murphy *et al.*, Phys. Rev. Accel. Beams **25**, 101301 (2022).
[31] A. Buck, K. Zeil, A. Popp, K. Schmid, A. Jochmann, S. D. Kraft, B. Hidding, T. Kudyakov, C. M. S. Sears, L. Veisz, S. Karsch, J. Pawelke, R. Sauerbrey, T. Cowan, F. Krausz, and U. Schramm, Rev. Sci. Instrum. **81**, 033301 (2010).
[32] B. Shahriari, K. Swersky, Z. Wang, R. P. Adams, and N. de Freitas, Proc. IEEE **104**, 148 (2016).
[33] C. K. Williams and C. E. Rasmussen, *Gaussian Processes for Machine Learning* (MIT Press, Cambridge, MA, 2006), Vol. 2.
[34] F. Pedregosa, G. Varoquaux, A. Gramfort, V. Michel, B. Thirion, O. Grisel, M. Blondel, P. Prettenhofer, R. Weiss, V. Dubourg, J. Vanderplas, A. Passos, D. Cournapeau, M. Brucher, M. Perrot, and E. Duchesnay, J. Mach. Learn. Res. **12**, 2825 (2011).
[35] A. Borzsonyi, A. P. Kovacs, and K. Osvay, Appl. Sci. **3**, 515 (2013).
[36] R. Lehe, M. Kirchen, I. A. Andriyash, B. B. Godfrey, and J.-L. Vay, Comput. Phys. Commun. **203**, 66 (2016).
[37] A. Lifschitz, X. Davoine, E. Lefebvre, J. Faure, C. Rechatin, and V. Malka, J. Comput. Phys. **228**, 1803 (2009).
[38] J. L. Vay, Phys. Rev. Lett. **98**, 130405 (2007).
[39] I. Moulanier, L. T. Dickson, C. Ballage, O. Vasilovici, A. Gremaud, S. Dobosz Dufrénoy, N. Delerue, L. Bernardi, A. Mahjoub, A. Cauchois, A. Specka, F. Massimo, G. Maynard, and B. Cros, Phys. Plasmas **30**, 053109 (2023).
[40] I. Moulanier, L. T. Dickson, F. Massimo, G. Maynard, and B. Cros, J. Opt. Soc. Am. B **40**, 2450 (2023).